Astronomy
&
Astrophysics

Special issue

Intensity contrast of solar network and faculae close to the solar limb, observed from two vantage points

K. Albert[1], N. A. Krivova[1], J. Hirzberger[1], S. K. Solanki[1], A. Moreno Vacas[2], D. Orozco Suárez[2],
N. Albelo Jorge[1], T. Appourchaux[3], A. Alvarez-Herrero[4], J. Blanco Rodríguez[5], A. Gandorfer[1],
P. Gutierrez-Marques[1], F. Kahil[1], M. Kolleck[1], R. Volkmer[6], J. C. del Toro Iniesta[2], J. Woch[1], B. Fiethe[7],
I. Pérez-Grande[9], E. Sanchis Kilders[5], M. Balaguer Jiménez[2], L. R. Bellot Rubio[2], D. Calchetti[1],
M. Carmona[8], W. Deutsch[1], A. Feller[1], G. Fernandez-Rico[1,9], A. Fernández-Medina[4], P. García Parejo[4],
J. L. Gasent Blesa[5], L. Gizon[1,10], B. Grauf[1], K. Heerlein[1], A. Korpi-Lagg[1], T. Lange[7], A. López Jiménez[2],
T. Maue[6,11], R. Meller[1], R. Müller[1], E. Nakai[6], W. Schmidt[6], J. Schou[1], J. Sinjan[1], J. Staub[1], H. Strecker[2],
I. Torralbo[9], and G. Valori[1]

(Affiliations can be found after the references)

ABSTRACT

Context. The brightness of faculae and network depends on the angle at which they are observed and the magnetic flux density. Close to the limb, the assessment of this relationship has until now been hindered by the increasingly lower signal in magnetograms.
Aims. This preliminary study aims to highlight the potential of using simultaneous observations from different vantage points to better determine the properties of faculae close to the limb.
Methods. We used data from the Solar Orbiter/Polarimetric and Helioseismic Imager (SO/PHI), and the Solar Dynamics Observatory/Helioseismic and Magnetic Imager (SDO/HMI), recorded at an ∼60° angular separation of their lines of sight at the Sun. We used the continuum intensity observed close to the limb by SO/PHI and complemented it with the co-observed $B_{\rm LOS}$ from SDO/HMI, originating closer to disc centre (as seen by SDO/HMI), thus avoiding the degradation of the magnetic field signal near the limb.
Results. We derived the dependence of facular brightness in the continuum on disc position and magnetic flux density from the combined observations of SO/PHI and SDO/HMI. Compared with a single point of view, we were able to obtain contrast values reaching closer to the limb and to lower field strengths. We find the general dependence of the limb distance at which the contrast is maximum on the flux density to be at large in line with single viewpoint observations, in that the higher the flux density is, the closer the turning point lies to the limb. There is a tendency, however, for the maximum to be reached closer to the limb when determined from two vantage points. We note that due to the preliminary nature of this study, these results must be taken with caution.
Conclusions. Our analysis shows that studies involving two viewpoints can significantly improve the detection of faculae near the solar limb and the determination of their brightness contrast relative to the quiet Sun.

Key words. Sun: photosphere – Sun: magnetic fields – Sun: faculae, plages

1. Introduction

The solar photospheric magnetic field is organised into the mainly weak-field low-lying loops forming the internetwork (found predominantly in the quiet Sun), which is almost invisible in white light, and kilogauss strength magnetic flux tubes that manifest themselves as dark sunspots and pores and bright faculae and quiet Sun network (see, e.g. Solanki et al. 2006). The brightness of a given flux tube (also often referred to as a magnetic element) depends on its size and the angle to the observer.

The horizontal pressure balance with the environment leads to an evacuation of the magnetic flux-tube interior, in order to maintain hydrostatic equilibrium in the presence of magnetic pressure. Therefore, for rays roughly parallel to the axis of the flux tube, the observable layer at optical depth $\tau = 1$ lies deeper than the surrounding photosphere. Whereas inside the flux tube the magnetic field inhibits convective energy transport, the walls of the flux tubes appear bright due to heating from the surrounding convection, the so-called hot wall effect (see, e.g. Spruit

1976). The balance between the lateral radiative heating and magnetic suppression of convection within a given flux tube depends on its diameter. Flux tubes tend to be close to solar surface normal due to magnetic buoyancy (see Buehler et al. 2015; Jafarzadeh et al. 2014). Therefore, the position of a flux tube on the observed solar disc determines which part of the flux tube we see, as a consequence of the angle at which we observe it. Going from the disc centre to the limb, the hot walls of the flux tubes rotate into view, before the edge closer to the observer starts to obscure the opposite, observer-facing wall (for extensive discussions, see Solanki 1993; Carlsson et al. 2004; Keller et al. 2004).

The small-scale flux tubes forming faculae and the magnetic network are typically not resolved by full-disc magnetographs, while the kilogauss flux tubes in the internetwork have so far only been resolved in exceptional cases, for example by Lagg et al. (2010) who used The Imaging Magnetograph Experiment magnetograph on the Sunrise balloon-borne solar observatory (e.g. Solanki et al. 2010; Barthol et al. 2011; Martínez Pillet et al. 2011). Thus, the size of faculae and

network elements is difficult to assess. Instead, the magnetic flux density within the resolution element (pixel) is often used to describe the fraction of the solar surface covered by strong fields (often referred to as the magnetic filling factor). The intrinsic field strength of the flux tubes forming a network and faculae is roughly unchanged, and their average size increases with the magnetic flux density. Therefore, it is also an indirect measure of the size of the magnetic features.

Determining the relationship between facular and network brightness and the magnetic flux density as well as the distance of the faculae from the solar limb is important for our understanding and modelling of the radiant properties and thermal structure of faculae and the magnetic elements of which they are composed. This also provides a classic constraint to magnetohydrodynamic simulations (see Beeck et al. 2015) and is relevant for studying and modelling the variations of solar irradiance at timescales of days to millennia, which is driven by the intensity excess created by faculae and the intensity deficit resulting from sunspots (see Krivova et al. 2003; Solanki et al. 2013; Shapiro et al. 2017; Yeo et al. 2017, 2020). In this study, we treat the facular and network features without differentiation, and refer to them as faculae collectively (Solanki & Stenflo 1984). Criscuoli et al. (2017) and Buehler et al. (2019) show benefits of treating them separately (see also Foukal et al. 2011), and this would be interesting to address in a future study building on the current one.

Numerous studies examined the intensity contrast of faculae (i.e. their intensity relative to that of the internetwork) in relation to their magnetic flux density (see Kobel et al. 2011; Kahil et al. 2019, and references therein), as well as their distance from the disc centre (see Ortiz et al. 2002; Yeo et al. 2013). For the magnetic flux density, most studies used the line-of-sight (LOS) magnetic field (B_{LOS}) observations, which is by far the most reliable of the magnetic components obtained from data utilising the Zeeman effect.

However, analysis of the facular contrast becomes complicated and very uncertain close to the solar limb for multiple reasons. Firstly, foreshortening effects become critical. Thus, since most of the observed magnetic field is nearly vertical, the B_{LOS} component becomes weak close to the limb leading to a low signal-to-noise ratio, which is further reduced due to lower light levels (limb darkening). In addition, the spatial resolution of observations is reduced, when approaching the limb, with each pixel representing an increasingly larger surface area on the Sun due to foreshortening. Within a pixel with larger coverage, the contribution of a given spatially unresolved magnetic element to the magnetogram signal and to the contrast of that pixel is smaller. Furthermore, the chances of opposite-polarity flux cancellation within such pixels are higher, resulting in lower magnetic flux density measurements.

Secondly, the μ value of the observation influences the observed height: closer to the limb, the absorption line in which the measurements are taken forms higher in the atmosphere than close to the disc centre (see Schou et al. 2023, for a discussion). Whereas this change in observation height is part of what we aim to observe in the intensity, it is an undesired effect in the case of B_{LOS} measurements, which are different to those carried out closer to the disc centre, distorting any comparisons between the two.

Thirdly, the incident polarised radiation from the Sun also depends on the angle of the observation, owing to the properties of the Zeeman effect. Due to radiative transfer effects and the finite width and geometry of solar magnetic features, the Stokes V amplitude need not scale linearly with μ (see Solanki et al. 1998). These additional effects include, but are not limited to, the following: (1) changes in the width and strength (including potential saturation) of the spectral line as a consequence of the lower temperature and increased turbulent velocities sensed by the line towards the limb; (2) possible changes in the Zeeman saturation of the Stokes V profile due to changes in field strength as a consequence of a greater formation height of the line and the larger inclination of the field relative to the LOS; and (3) the passage of individual rays through both magnetised and unmagnetised gas, etc.

Fourthly, the identification and isolation of facular features is also more challenging close to the limb because the apparent extension of the magnetic canopy of sunspots increases towards the limb (Giovanelli & Jones 1982; Solanki et al. 1994). As the canopy contributes significantly to Stokes V, it can be mistaken for a facular contribution (see Yeo et al. 2013; Ball et al. 2012).

Because of these restrictions, studies of the contrast of bright magnetic features are typically curtailed near the solar limb. For example, Yeo et al. (2013) studied the facular intensity contrast as a function of distance from the disc centre (in terms of the cosine of the heliocentric angle, denoted as $\cos\theta = \mu$) and the measured magnetic flux density, normalised by μ (B_{LOS}/μ), using data from the Helioseismic and Magnetic Imager on board the Solar Dynamics Observatory (SDO/HMI, see Schou et al. 2012). (The normalisation by μ corrects for the geometrical effects to first order under the assumption that the field is vertical to the local solar surface). Due to the factors discussed above, weak network features ($B_{\mathrm{LOS}}/\mu < 50\,\mathrm{G}$) could not be identified in the magnetograms near the limb ($\mu \leq 0.4$), so that the centre-to-limb variation (CLV) of facular intensity contrast in this regime remains unclear.

These restrictions could be overcome (or at least their severity reduced) if, in addition to a magnetograph on the ground, or in Earth's orbit, a second such instrument observing the Sun from a different viewpoint were available. The Solar Orbiter mission (Müller et al. 2020) brings this new perspective to solar observations: it reaches a wide range of positions outside the Sun-Earth line and it carries the Solar Orbiter/Polarimetric and Helioseismic Imager (SO/PHI; Solanki et al. 2020), the first solar magnetograph to provide data with significant angular separations from Earth. A combined analysis of simultaneous observations by SO/PHI and on-ground or Earth orbiting instruments presents an opportunity to examine the Sun from two perspectives simultaneously. In particular, this allows the uncertain B_{LOS} measurements at the limb to be substituted with more certain ones, inferred from observations closer to the disc centre, hence improving on earlier studies of facular contrast.

In this study, we present such an effort. To highlight the potential of such multi-angle studies to better constrain the dependence of facular brightness on the measured magnetic flux density and the distance to the limb, we combined simultaneous observations from SO/PHI and SDO/HMI (Schou et al. 2012). We stress that we do not aim to provide final results. Instead, this study demonstrates that such a combination of viewpoints can indeed improve our knowledge of facular contrast, in particular close to the solar limb.

The paper is structured as follows. We present our method in Sects. 2 and 3 by first detailing the observations from SO/PHI and SDO/HMI and their processing, and then by describing how we combined the two vantage points. In Sect. 4, we explain how we derived the relationship of the facular contrast to μ and B_{LOS}/μ from the combined data obtained by the two instruments, and from SO/PHI's perspective alone; we then provide a discussion. In Sect. 5 we summarise our findings and discuss how the obtained results can be improved and extended in the future.
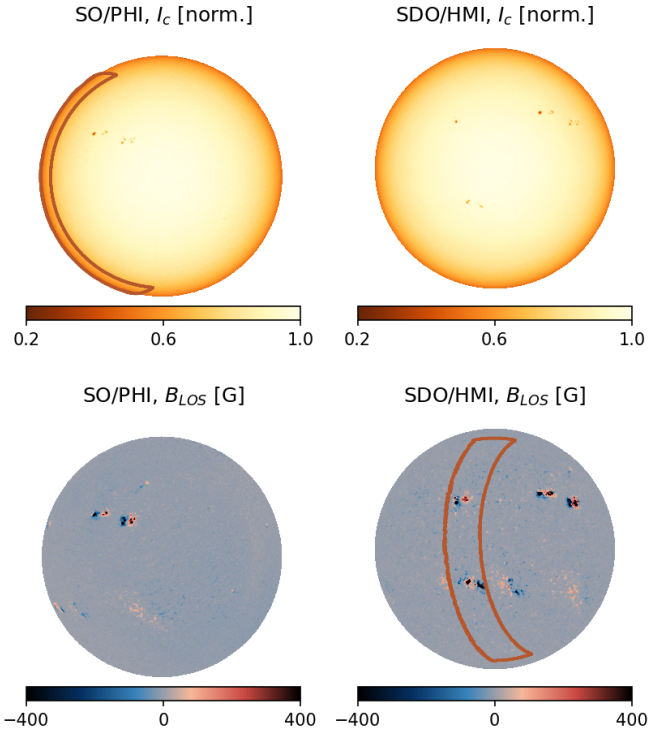
Fig. 1. Co-observations of the two instruments. We show I_c (upper row) and B_{LOS} (lower row) observed by SO/PHI full disc telescope (FDT, left column) and SDO/HMI (right column), on 6 September 2021. The two instruments observed the Sun with 59.45° angular separation. The brick-red outlines on the panels show the regions that we combined for the analysis: I_c from SO/PHI and B_{LOS} from SDO/HMI within the overlap region of the two instruments, with $0.1 < \mu_{SO/PHI} < 0.4$ and $\mu_{SDO/HMI} > 0.4$.

2. Data and their processing

2.1. Data

The SO/PHI (Solanki et al. 2020) is an imaging spectropolarimeter, sampling the photospheric Fe I 617.3 nm absorption line. It has two telescopes: the Full Disc Telescope (FDT) and the High Resolution Telescope (HRT, see Gandorfer et al. 2018). As their names suggest, the FDT covers the full solar disc at all phases of the spacecraft's orbit (with a pixel plate scale 3.75″), while the HRT only images a fraction of it (pixel plate scale 0.50″). The SO/PHI measures the full Stokes vector (I, Q, U and V) at six wavelength positions: five inside the spectral line, and one in the nearby continuum. From these, through the Zeeman and Doppler effects, the vector magnetic field ($\boldsymbol{B}$) and the LOS velocity (v_{LOS}) can be determined at the average formation height of the spectral line. In addition, the continuum intensity is also returned. In this study, we use data products obtained in the longitudinal mode of the SO/PHI instrument. This is a simplified mode, which is applied on board to reduce processing time and telemetry volume (see Albert et al. 2020). It provides the continuum intensity (I_c), and B_{LOS} (instead of $\boldsymbol{B}$), calculated with analytical formulae via the centre-of-gravity technique (Semel 1967; Rees & Semel 1979; Landi Degl'Innocenti & Landolfi 2004). These results are referred to as classical estimates. The measurement duration for a full data set is approximately 33 s.

The SDO/HMI observes the same absorption line, using the same principle. Some relevant differences between the instruments are the pixel plate scale (0.505″ for SDO/HMI), the sampling wavelengths of the line (SDO/HMI's six wavelength samples are uniformly spaced and centred over the line, sometimes resulting in the continuum not being directly sampled), and while it provides similar data products, it uses somewhat different techniques to derive them. Here we use the 720 s data products: the reconstruction of continuum intensity, and the LOS magnetogram (hmi.M_720s; calculated with the MDI-like algorithm, see Couvidat et al. 2016).

We use 10 pairs of SO/PHI–SDO/HMI observations, recorded during the cruise phase of SO, one from each day in the period 1 to 10 September 2021. The SO/PHI data used in the study is of the full solar disc, recorded with the FDT. During the observations, the angular separation of the two instruments changed from 67° to 52°, while SO's distance to the Sun varied from 0.58 AU to 0.60 AU. The SO/PHI-FDT at these distances observes the Sun with a radius of 440 to 453 pixels. The SO/PHI data have been fully reduced on board the spacecraft, including the calibration and the determination of B_{LOS} (for details of the onboard processing see Albert et al. 2020). Due to the early phase of the mission, and the novelty of the onboard data processing, the calibration data and processes applied during the reduction of these data sets are preliminary.

Since we are mainly interested in extending earlier studies of facular contrast to locations closer to the solar limb, we analyse areas that appear at $0.1 < \mu < 0.4$ in SO/PHI data, and at $\mu > 0.4$ in SDO/HMI data. As an example, Fig. 1 shows I_c and B_{LOS} from co-observations of SO/PHI and SDO/HMI on 6 September 2021. The regions that we analyse lie within the brick-red contours: the I_c at the limb from SO/PHI, and the corresponding area in the SDO/HMI B_{LOS} at large μ values. We remark that combining the data the other way around, that is taking I_c from SDO/HMI (from the limb), and complementing them with B_{LOS} from SO/PHI (closer to disc centre) would also be possible. However, such a combination is expected to be less accurate, as we have higher noise levels in the SO/PHI magnetograms (due to e.g. the lower amount of temporal averaging).

2.2. Attuning the observations

To prepare the SDO/HMI data products for combination with SO/PHI data, we convolve them with the point spread function (PSF) of the SO/PHI-FDT. As results of more accurate studies were not yet available, we used a theoretical PSF: the Airy disc of the telescope. This assumes a perfect telescope, only limited by the diffraction of light. To arrive at the effective PSF, we adjust this to the difference in distance to the Sun of the two instruments. Due to the large difference in aperture size (140 mm in SDO/HMI vs. 17.5 mm in SO/PHI-FDT) which is not nearly compensated by the difference in distance to the Sun (1 AU for SDO/HMI and 0.6 AU for SO/PHI), we consider the SDO/HMI PSF to be negligible relative to that of SO/PHI. More accurate PSF estimates, available now (see Bailén et al. 2023; Kahil et al. 2023), will be used in subsequent studies.

Next, we resample the SDO/HMI data to match the spatial sampling of the SO/PHI-FDT observations (i.e. we bin the SDO/HMI data by a non-integer factor). We achieve this in the Fourier domain. We crop the convolved data (conserving the lower frequency regions) to a dimension which after the inverse

transform will provide the same solar radius in pixels as we observe in the corresponding SO/PHI data set.

For our analysis, the B_{LOS} values come exclusively from SDO/HMI observations (degraded and resampled to mimic SO/PHI), while the intensity contrast values are exclusively from SO/PHI. Thus, in principle, we do not need to worry about the magnetic and continuum intensity cross-calibration of the two instruments. However, the cross-calibration might have an effect on the comparison of the results obtained from combining the two viewpoints with those obtained from SO/PHI only, and can therefore affect our results presented in Fig. 5 (see Sect. 4). We see a good continuity of the results, and therefore believe that for the scope of this pre-study we can use data that have not been cross-calibrated. Efforts to cross-calibrate SDO/HMI and SO/PHI-FDT data products are underway (Vacas 2022, priv. comm.), and should be used by future studies.

2.3. Identification of faculae

We identify faculae or network, sunspots or pores, and internetwork following the method described by Yeo et al. (2013; for a discussion on the effects of identification methods, see Centrone & Ermolli 2003). This is done for both instruments individually. In the case of SDO/HMI, we use the PSF-degraded and resampled data. Faculae or network are identified in the magnetograms by their elevated B_{LOS} levels, while sunspots or pores are identified in the I_{c} images by lower intensity levels. Finally, parts of the Sun that do not qualify to be either network, faculae, sunspot, or pore are counted as internetwork.

We first detect pixels with magnetic signals sufficiently above the noise level of the B_{LOS} maps:

$$B_{\text{LOS}}(x, y) > 3\sigma_{B_{\text{LOS}}}(x, y), \tag{1}$$

where x and y are detector plane coordinates, B_{LOS} is the measured LOS magnetic field, and $\sigma_{B_{\text{LOS}}}$ is the standard deviation of B_{LOS}, a measure of the noise in B_{LOS}.

We determined $\sigma_{B_{\text{LOS}}}$ following the method described by Ortiz et al. (2002) and Yeo et al. (2013). This method includes two steps: (1) a computation of the CLV of the noise, and (2) a computation of the deviations from the obtained noise CLV profile. Thus, we first calculated the standard deviation, σ, of the magnetogram signal over concentric rings of pixels at similar distances from the disc centre and removed outliers, outside 3σ, iteratively, until convergence. We also fitted a polynomial to the standard deviation versus distance profiles, thus establishing the CLV noise profiles. Afterwards, we used a moving window to determine any deviations from the CLV noise profile, and fitted a polynomial surface to the result. We note, that if a window contains mostly active region pixels, the standard deviation within it is higher than for a quiet Sun region. Therefore, our noise levels should rather be considered as an upper limit. We prefer this conservative approach, where we may miss some facular pixels, over the potential inclusion of some noise in the analysis.

When we apply this method to the 720 s SDO/HMI magnetograms at their original resolution, our approach returns the noise level 4 to 7 G. This is close to the values of 4.7 to 7.8 G reported by Liu et al. (2012). We note that the SDO/HMI team used more accurate methods to determine the noise level than we do. After changes in the processing of the 720 s magnetograms in 2016, these values are expected to be somewhat lower (Liu 2022, priv. comm.). Through analysing internetwork pixels, Korpi-Lagg et al. (2022) found ~5.5 G noise levels prior to 2016, and ~4.75 G afterwards.

For the resampled SDO/HMI magnetograms, we find the noise level in the range from 3.5 to 5.2 G. The downsampling of the data by nearly a factor of four, that is averaging over ~16 pixels, does not reduce the noise level by a factor of four. This reduction would be expected if the photon noise were the only noise source, however, that is not the case for the 720 s HMI LOS magnetograms (see Liu et al. 2012). Moreover, at the resulting resolution, while quiet Sun weak magnetic fields are visible, they are wrongly classified as noise. This again leads to a conservative pixel classification, as we potentially exclude some pixels from the analysis which harbour network magnetic fields.

In the case of the SO/PHI magnetograms, the variation of the noise level over the field of view does not show a clear CLV. Instead, it is dominated by a large-scale gradient across the field of view, the origin of which is still under investigation. This indicates that also for SO/PHI, the noise level is not driven by photon noise only. In the absence of a clear CLV of the noise profile for the SO/PHI magnetograms, we calculate the noise directly with the moving window. This yields noise levels ranging from 7.1 G to 10.4 G, which is higher than what we find in the resampled SDO/HMI data.

Next, we identified the pixels that belong to sunspots or pores based on I_{c}. To achieve this, we first calculated the CLV of the quiet Sun at the continuum wavelength following the method described by Neckel & Labs (1994). We then found the large-scale deviations of the quiet Sun I_{c} from the CLV, which we consider to be a residual of the flat field correction, following Yeo et al. (2013). The SO/PHI I_{c} observations are subject to a ghost image, which is a faint (~0.5% of the intensity) duplicate image of the Sun overlaid on the solar disc with a small spatial offset. Therefore, we first mitigated the effect of this ghost image on the sensor, and then determined the residuals on the result.

We normalised I_{c} by its CLV and the flat field residuals:

$$I_{\text{c,norm}}(x, y, t) = \frac{I_{\text{c}}(x, y, t)}{\text{CLV}_{I_{\text{c}}}(x, y) R_{I_{\text{c}}}(x, y)}, \tag{2}$$

where t is time (which refers to one of the 10 considered data sets), $I_{\text{c,norm}}$ denotes the normalised I_{c}, $\text{CLV}_{I_{\text{c}}}$ denotes the centre to limb variation of the quiet Sun intensity, and $R_{I_{\text{c}}}$ marks residuals of the flat field correction, present in the I_{c} data.

To obtain an intensity threshold for identifying sunspots, we again followed Yeo et al. (2013). For the 10 data sets, we derived the quiet Sun $I_{\text{c,norm}}$ standard deviation, which we denote $\sigma_{I_{\text{c}},\text{QS}}$. The threshold separating sunspots from the internetwork ($I_{\text{c,threshold}}$) was set, conservatively, at the mean of the minimum value of $I_{\text{c,norm}}(x, y, t) - 3\sigma_{I_{\text{c}},\text{QS}}(x, y, t)$ for each of the 10 days. The $I_{\text{c,threshold}}$ is 0.965 in SO/PHI, and 0.975 in SDO/HMI. We consider all pixels below these values to belong to sunspots or pores.

As a final step in our pixel segmentation, we found all isolated pixels identified as faculae based on the previous criteria. We considered these to be false positives, and therefore treated them as internetwork fields.

Figure 2 shows the distribution of the pixels of interest derived from the magnetograms of both instruments. The top panels show B_{LOS}/μ at various μ values, while the bottom panels show I_{c}. The SO/PHI I_{c} (bottom left panel) shows a weak downward trend when approaching the limb, indicating a bias in the normalisation of I_{c}. This is a result of imprecision in determining the radius of the Sun in the images, mainly due to two factors: low spatial resolution, and the as yet uncorrected distortion of the SO/PHI-FDT. In SO/PHI magnetograms, where the region was close to the limb, we find 853 facular pixels, which is
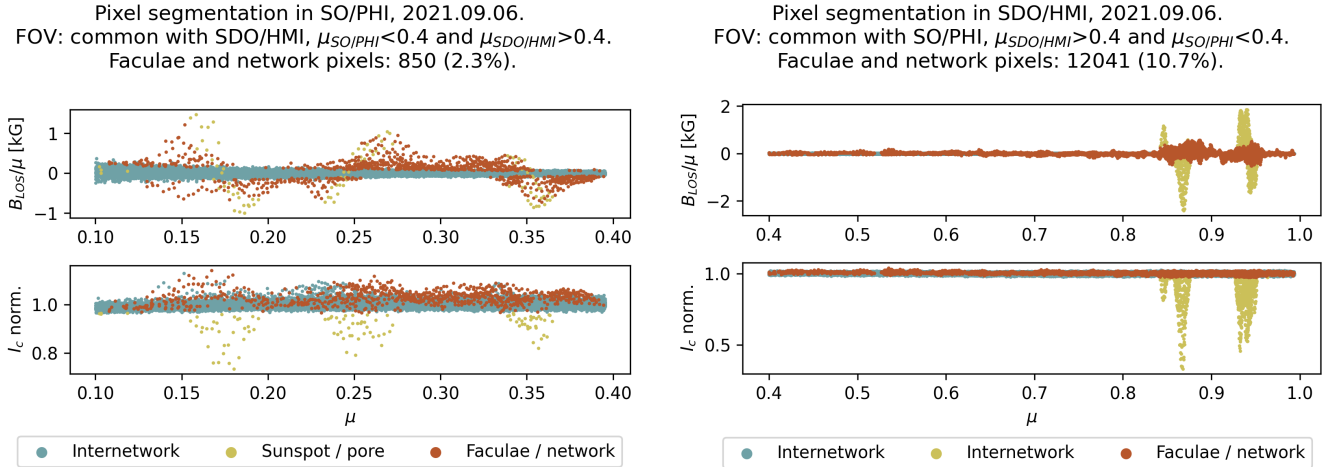
Pixel segmentation in SO/PHI, 2021.09.06.
FOV: common with SDO/HMI, $\mu_{SO/PHI}<0.4$ and $\mu_{SDO/HMI}>0.4$.
Faculae and network pixels: 850 (2.3%).

Pixel segmentation in SDO/HMI, 2021.09.06.
FOV: common with SO/PHI, $\mu_{SDO/HMI}>0.4$ and $\mu_{SO/PHI}<0.4$.
Faculae and network pixels: 12041 (10.7%).

Fig. 2. Classification of pixels within the common area of interest in both instruments. We show pixels from the region $0.1 < \mu_{\mathrm{SO/PHI}} \leq 0.4$ and $\mu_{\mathrm{SDO/HMI}} > 0.4$, and their distribution with μ from images recorded on 6 September 2021. In this field of view, we identify 2.2% of the SO/PHI pixels (close to limb) and 6.2% of SDO/HMI pixels (closer to disc centre) as faculae.

2.2% of all pixels in this area. In the resampled SDO/HMI data, where the region appeared closer to the disc centre, we identify 12 041 pixels as faculae, that is 10.7% of all pixels in this area. The difference in the fraction of pixels identified as faculae is due to the combined effect of three factors. (1) The noise level in the SDO/HMI data is lower than that in SO/PHI. (2) The signal-to-noise ratio of the B_{LOS} measured close to the disc centre is higher than that measured closer to the limb. (3) Due to the foreshortening effect, pixels close to the limb represent a larger surface area on the Sun, which leads to more averaging and thus more potential cancellation of oppositely signed magnetic flux (in SO/PHI data) as compared to pixels recorded closer to the disc centre (HMI data).

The produced maps that mark the locations of the facular pixels were then used for our analysis (see Sect. 4).

2.4. Definition of the intensity contrast

Following Yeo et al. (2013), we calculate the continuum intensity contrast of the facular pixels. We define C_{I_c}, as:

$$C_{I_c}(x, y, t) = I_{\mathrm{c,norm}}(x, y, t) - 1, \tag{3}$$

where $I_{\mathrm{c,norm}}(x, y, t)$ is defined in Sect. 2.3.

3. Combining the two vantage points

Our goal here is to assign to each I_c pixel measured by SO/PHI at the limb the corresponding B_{LOS}/μ value measured by SDO/HMI closer to the disc centre. The close-to-centre SDO/HMI measurements are a 'super-sampled' version of what SO/PHI measured close to limb: due to foreshortening, several pixels at a large μ value combine into a single one at the limb (i.e. the spatial coverage of the pixels increases). Thus, to assign the SO/PHI limb pixels with the B_{LOS}/μ values measured by SDO/HMI, we first need to cross-match the pixels in the observations by the two instruments, that is, we have to find which B_{LOS}/μ pixels in SDO/HMI correspond to the I_c pixels measured by SO/PHI. To do this co-alignment, we re-projected the SDO/HMI B_{LOS}/μ data to the coordinate system of SO/PHI, using the SunPy (see SunPy Community 2020) implementation of the method described in DeForest (2004). This method uses a Hanning window to weigh the input pixels in the footprint of

each output pixel, reducing aliasing effects, and producing values close to the mean. Thereby, the mean of B_{LOS}/μ over the input pixels is (roughly) preserved in the output pixel. We additionally correct for the time difference in the data acquisition of the two instruments and the difference in the light travel time, by considering the differential rotation of the Sun (method from Howard et al. 1990, also implemented in SunPy).

To improve data alignment and correct for any shift originating from small inaccuracies in our knowledge of the observing geometry (described in World Coordinate System, coordinates, see Thompson 2006), we derive and apply a preliminary distortion model to the re-projected data. This distortion model is based on the pixel to pixel local correlation of the B_{LOS}/μ by SO/PHI and the re-projected measurements of it by SDO/HMI in the overlapping area. From the cross-correlation values, we derive a map giving the correct position of each pixel. Such an empirical method is susceptible to errors due to noise. Therefore, to minimise these errors, we fitted a second order polynomial surface to the resulting map. We apply the derived distortion model to the SDO/HMI data after re-projecting it, instead of correcting the distortion in the SO/PHI measurements. This decision was taken here to preserve the intensity contrast observed at the limb, as methods readily available to correct the SO/PHI data, based on interpolations, lower it. To illustrate the quality of the data alignment, Fig. A.1 shows an example of a co-aligned SO/PHI and SDO/HMI region together with cross-sections of B_{LOS}/μ through the region.

We also re-project the facular map found in the SDO/HMI magnetogram close to the disc centre (see Sect. 2.3) with the method used for B_{LOS}/μ, to SO/PHI's coordinate system, and align the result with the distortion model described above. This re-projected SDO/HMI-based facular map consists of pixels that have varying amount of contribution from pixels identified as facular in the original SDO/HMI data (before re-projection). In order to make sure that we analyse pixels that behave as faculae (i.e. the facular contribution is not insignificant compared to the internetwork contribution), we set a threshold based on B_{LOS}/μ. We included in our analysis only those re-projected pixels that have the resulting B_{LOS}/μ above the 3σ noise level of the SO/PHI-FDT (in line with the identification process of faculae that we used earlier, see Eq. (1)). This is a conservative threshold, and we might miss some faculae that could be considered,
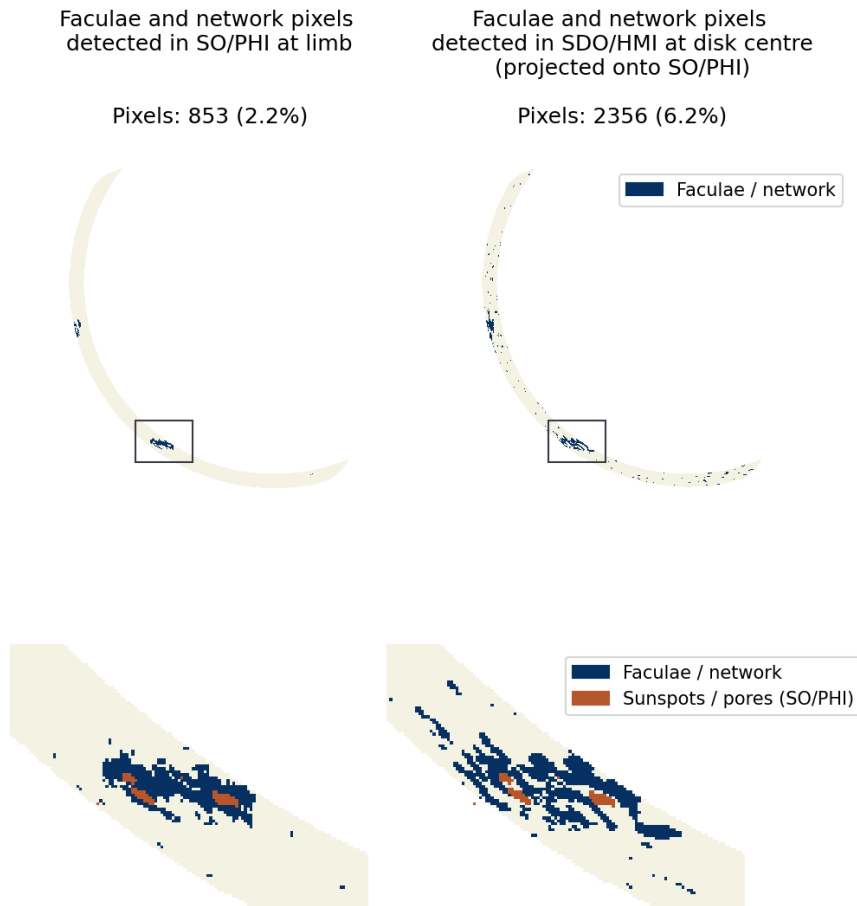
Faculae and network pixels
detected in SO/PHI at limb

Faculae and network pixels
detected in SDO/HMI at disk centre
(projected onto SO/PHI)

Pixels: 853 (2.2%)

Pixels: 2356 (6.2%)

Fig. 3. Faculae map identified in SO/PHI (left) and in SDO/HMI, re-projected to the coordinate system of SO/PHI (right). The upper row shows the area analysed in the study, the lower row shows a magnification of the area marked by the black rectangle on the top. In the magnified view, we also show the area that was identified as sunspot in the SO/PHI observations. We indicate the number of pixels identified as faculae in each figure (853 in SO/PHI, and 2356 in SDO/HMI, representing 2.2% and 6.2% of the pixels in this area, respectively). The data shown here are from 6 September 2021.

however for this study we prioritise the avoidance of false positives over the inclusion of all facular pixels. At the same time, we can now consider even stand-alone pixels as correct identification, as they were observed in several SDO/HMI pixels close to the disc centre. Furthermore, we exclude any pixels that have contributions from sunspots or pores, as the measured intensity would be strongly affected by these features. The resulting facular map shows significantly more facular pixels near the limb than the SO/PHI-FDT magnetogram. Figure 3 compares the faculae maps obtained at the limb using SO/PHI data and at large μ from SDO/HMI data, projected in the figure onto SO/PHI's coordinates. The 12 041 facular pixels, identified close to the disc centre in the resampled SDO/HMI magnetograms (from Fig. 2), convert into 2356 pixels at the limb. The facular features at the limb, found through the re-projection of the SDO/HMI facular map, represent 6.2% of all the pixels in this region, compared to 2.2% for those obtained directly from the SO/PHI limb data. This increase in the percentage of pixels identified close to limb with the data from disc centre indicates that many faculae with small flux density have been systematically missed at the limb in previous studies. However, the re-projection of the SDO/HMI facular map shows fewer faculae in the close surroundings of sunspots. This has to do with the extended magnetic canopies of sunspots. In the near-limb SO/PHI observations, the magnetic canopy of the sunspot appears particularly extended (particularly in $B_{\rm LOS}$), leading to sunspots being surrounded by pixels displaying a high magnetic flux density. These pixels are falsely identified as faculae in the SO/PHI facular map, whereas in the SDO/HMI facular maps the same region

is located at high μ, and the canopies produce at most a very weak $B_{\rm LOS}$ signal close to the sunspot, which is not mistaken for faculae.

By inferring the $B_{\rm LOS}$ at low μ values from the re-projection of the same areas measured at a higher μ, we reduce the uncertainty in the $B_{\rm LOS}$ values measured close to the limb. We circumvent the problems arising at the limb, including the diminishing LOS component, lower light levels, increasing pixel coverage, changes in the formation height of the line, the radiative transfer effects, and the apparently extended sunspot canopy affecting faculae identification.

Our analysis involves a number of assumptions and approximations. Firstly, in our re-projection, we approximated the solar surface as a plane, ignoring any obstructions that occur in our line of sight due to the undulated solar surface. This could lead to cases where we identify faculae close to the disc centre, which are, however, obstructed by solar granulation closer to the limb. Such possible pixels would exhibit the intensity (and magnetic field) of internetwork at the limb, and, therefore, could bias the analysis towards lower contrast levels. Secondly, we considered the studied flux tubes to be vertical with respect to the solar surface, and therefore assumed that a normalisation by μ accounts for the foreshortening. Thirdly, we assumed that the different wavelength sampling of the spectral line, the somewhat different data reduction codes used to retrieve the $B_{\rm LOS}$, and the different observation time (over 720 s for SDO/HMI, and 33 s for SO/PHI) provide equivalent results. All of these assumptions might have an effect on our results and should be considered further in future studies.
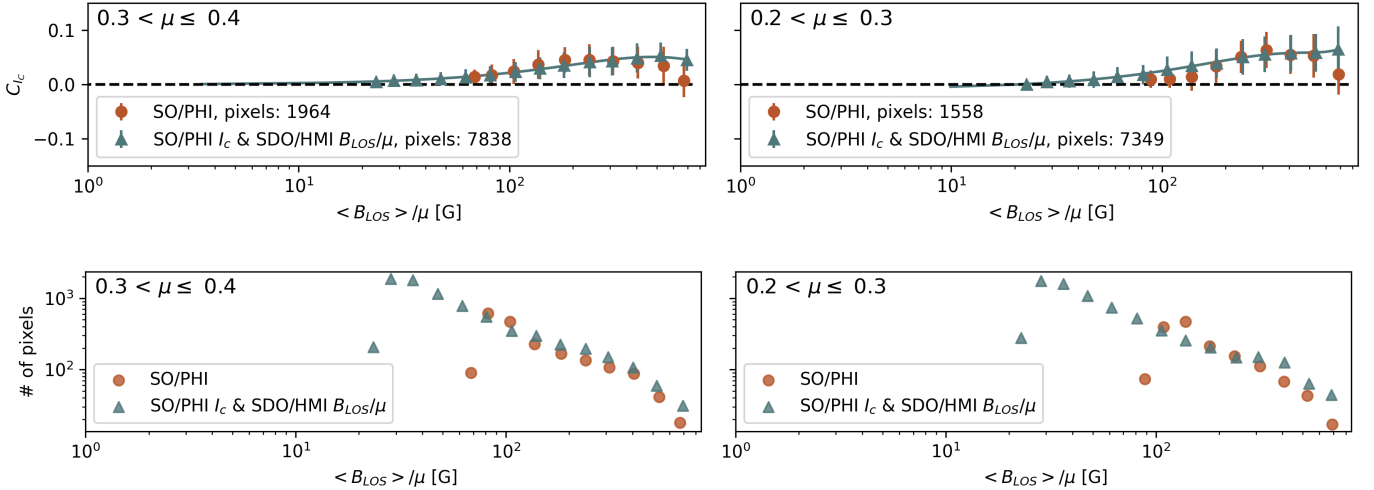
Fig. 4. Facular contrast as a function of B_{LOS}/μ, and the number of pixels in each bin. Top: we computed the contrast curves using the combined SO/PHI and SDO/HMI data as well as the SO/PHI data alone in two μ intervals ($0.1 < \mu \leq 0.3$, right column, and $0.3 < \mu \leq 0.4$, left column). We split the data into equal intervals of $\log(B_{LOS}/\mu)$. The error bars represent the standard deviation of the pixels within each bin. We fitted a third order curve to the combined data points (continuous green line). Bottom: based on the number of pixels in each bin, we exclude from the plots SO/PHI-based data with $\mu < 0.2$.

4. Results and discussion

The intensity contrast depends on both the location of the feature on the disc and the magnetic field strength averaged over the pixel. To disentangle the dependence of C_{I_c} on each of these two factors, we consider individual μ and B_{LOS}/μ intervals following Ortiz et al. (2002).

First, we consider the dependence on B_{LOS}/μ. We first split all data into two μ intervals ($0.1 < \mu \leq 0.3$ and $0.3 < \mu \leq 0.4$) and look at the dependence of the contrast on B_{LOS}/μ in each of them. In each interval, we bin the data into 14 equal intervals of $\log(B_{LOS}/\mu)$, and compute the bin-averaged C_{I_c} (see Fig. 4). The standard deviation within the bins is shown in the figure as error bars. The two curves show the intensity contrast derived exclusively from SO/PHI data (brick-red markers), and from the combined measurements (i.e. C_{I_c} from SO/PHI and B_{LOS} from SDO/HMI re-projected to the coordinate system of SO/PHI, as described in Sect. 3, shown in pine-green symbols). We show data with $\mu > 0.1$ for the combined measurements, and with $\mu > 0.2$ for SO/PHI-only data. The restriction to $\mu > 0.2$ for these data is due to the low signal-to-noise ratio in the SO/PHI magnetograms at $\mu \leq 0.2$. We plot the number of data points entering each $\langle B_{LOS} \rangle$ bin, separately, in the bottom panels. When using the SO/PHI data alone, the weakest regions we could detect at $\mu < 0.4$ were those with roughly $B_{LOS}/\mu \approx 80-90$ G. By using the combined data, we could extend our analysis to regions as weak as $B_{LOS}/\mu \approx 20$ G.

Earlier studies found that, in regions not extremely near to the limb, the contrast of facular features initially increases with B_{LOS}/μ, then usually decreases again at yet higher B_{LOS}/μ values (see e.g. Ortiz et al. 2002; Yeo et al. 2013). Although the error-bars are rather high, we see a similar tendency in the top-left panel of Fig. 4, too. At the same time, closer to the limb, the contrast of faculae keeps increasing with increasing magnetic flux density (see the top-right panel), also in agreement with previous studies. This behaviour is due to the fact that for larger facular features (or pores) produced by stronger magnetic fields, we see increasingly more of the darker central part of the flux tube when approaching the disc centre, similarly to sunspots. Near the limb, we see more of the hot walls, so that all features are bright.

Similarly, we then split all the data into six B_{LOS}/μ intervals and derive the dependence of the contrast on μ within each of these individual ranges (see Fig. 5). Our results suggest that studies involving two vantage points (such as this one) have the largest impact on pertaining to faculae with lower flux density. Therefore, we choose smaller intervals for the lower B_{LOS}/μ range, and group a larger range into one interval for the higher flux densities. Another driver of this choice are the few magnetograms used in this study, which mean that there are relatively few pixels showing large flux densities. Within each interval, we created bins that are $\Delta\mu = 0.05$ wide and calculate the mean intensity contrast in each (for reference, the widest pixel in the analysed area covers $0.02\,\mu$). Again, by combining data from two viewpoints (in pine-green), we significantly extend the μ range beyond what was possible with data from a single perspective (in brick-red), especially at low B_{LOS}/μ.

The determination of the distance from disc centre, where the facular contrast is highest (μ_{max}), has been a long-standing debate in facular studies (see Solanki 1993). To determine the μ_{max} in our contrast curves, we fitted a third order polynomial to the bins calculated from the combined SO/PHI and SDO/HMI observations at $\mu \leq 0.4$, and from SO/PHI only data at $\mu > 0.4$ (see Fig. 5). We calculated μ_{max} based on the obtained fit, and compare our values to those reported in earlier studies by Ortiz et al. (2002) and Yeo et al. (2013) in Table 1. We find the trends in μ_{max} with changing B_{LOS}/μ to be similar to what earlier studies observed, which is the increase of μ_{max} with decreasing magnetic flux density. However, we do not observe the inversion of this trend for the weakest flux densities. Our μ_{max} values are also on average somewhat lower than those found by Ortiz et al. (2002) and Yeo et al. (2013). We must consider, however, that the resolution of our data is lower than of that used in the compared studies. Another difference to these studies is the B_{LOS}/μ intervals in which we derive μ_{max}. We note, however, that repeating the analysis for the intervals used by Yeo et al. (2013) and Ortiz et al. (2002), yielded no significant difference in the results.

Our extension of the observed μ range for low B_{LOS}/μ values compared to the SO/PHI-only contrast curves indicates that combining two vantage points leads to more accurate μ_{max} in
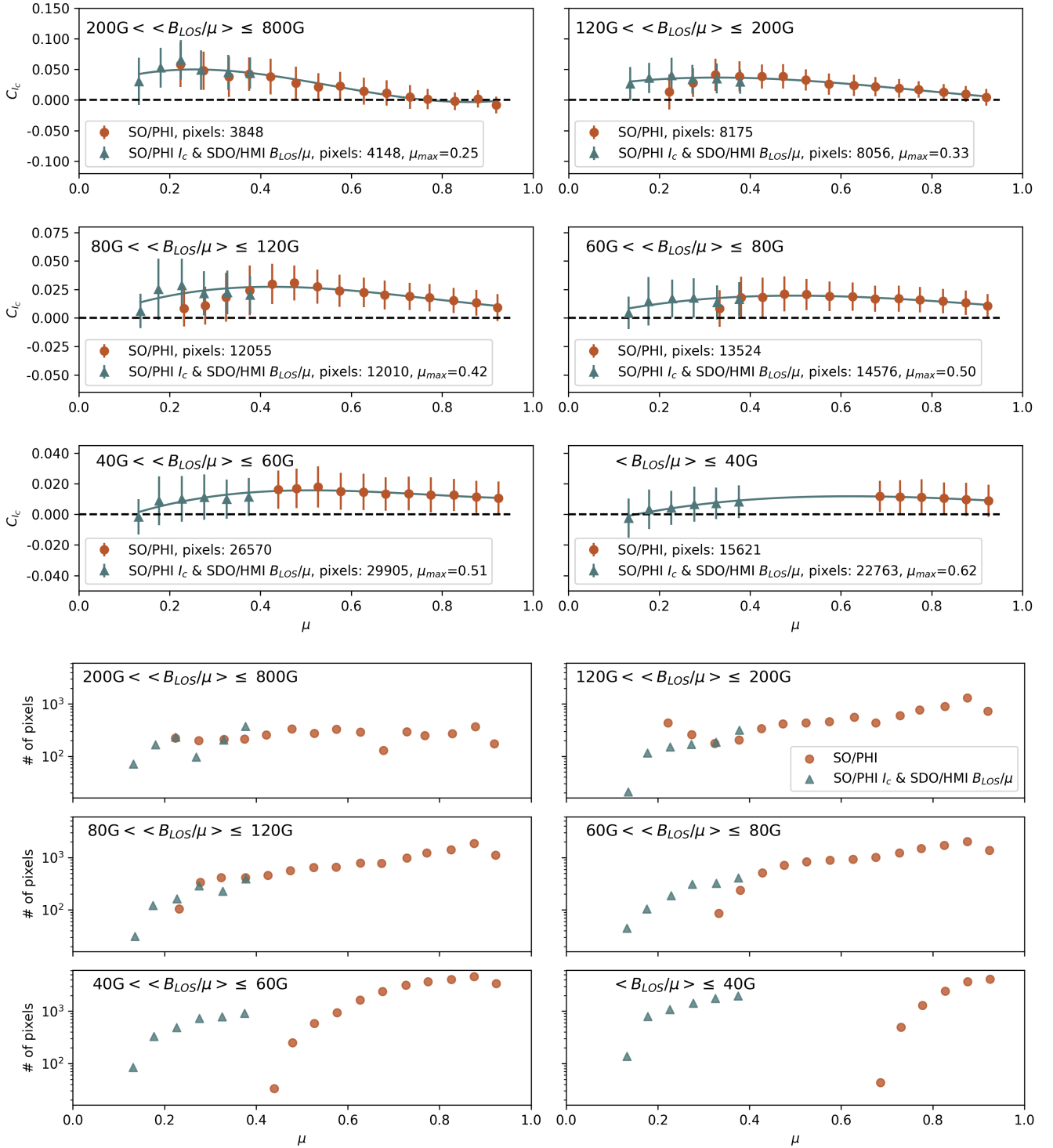
Fig. 5. Same as Fig. 4, but now showing facular contrast vs. μ. The data are displayed in six intervals of B_{LOS}/μ, and in bins of $\Delta\mu = 0.05$. The third order fit here is done through the combined points, extended with the points derived from SO/PHI only data where $\mu > 0.4$.

such regions than enabled by single viewpoint observations. To this end, however, more and higher spatial resolution data are needed to be analysed than what is considered in the present study. Due to the large error bars in our results, which are the consequence of the provisional nature of the data, their low resolution, the low statistics (only ten days of observations), and possible biases related to the normalisation of the I_c as a consequence of the low resolution and distortion, our results must be considered preliminary.

5. Conclusions and outlook

One of the unprecedented opportunities offered by Solar Orbiter is that by co-observing together with other spacecraft in Earth's orbit, we have the possibility to observe the properties of a given region on the solar surface from two different vantage points. In this work, we use co-observations of SDO/HMI and SO/PHI, with an approximately 60° angle between their LOS, to study the dependence of facular brightness on the magnetic field strength

Table 1. Values of μ_{max} calculated for various B_{LOS}/μ ranges in this work, compared to what Yeo et al. (2013) and Ortiz et al. (2002) find.

B_{LOS}/μ [G]	This study	Yeo et al. (2013)	Ortiz et al. (2002)
<40	0.62		
<50		0.38	0.50
40–60	0.51		
50–80			0.55
60–80	0.50		
50–100		0.45	
80–120	0.42		0.50
100–180		0.45	
120–200	0.33		0.49
180–280		0.40	
200–300			0.42
280–380		0.38	
300–400			0.42
380–500		0.36	
400–500			0.35
200–800	0.25		
500–600			0.22
500–640		0.33	
640–800		0.29	

and μ close to the solar limb. Earlier such studies faced the problem of strongly reduced magnetogram signals when measuring the LOS component of the magnetic field close to the limb. This is because of two main effects. Firstly, most of the field emerging in facular and network regions is roughly aligned with the solar surface normal, so that towards the limb its LOS component becomes increasingly weak, eventually falling below the instrumental noise level. Secondly, due to the reduced spatial resolution at the limb produced by foreshortening, the in-pixel averaging and cancellation effects of the measured flux density become more important. The combination of these effects, together with others (e.g. increased noise near the limb and the apparent extension of the magnetic canopy of sunspots), make it harder to detect faculae via their magnetic signature near the solar limb. Therefore, to measure the continuum intensity contrast in facular regions close to the limb, we combined SO/PHI continuum intensity measured close to the solar limb with the magnetic field co-observed by SDO/HMI closer to the disc centre. Based on these data, we derived curves that describe the intensity contrast of facular pixels in relation to their position on the solar disc (expressed in μ) and to their magnetic flux density (observed as B_{LOS}, and normalised to μ to counteract geometrical effects).

The preliminary results presented here highlight the potential of combining data from different angles. In particular, such a combined approach allows for more reliable B_{LOS}/μ measurements for areas with $0.1 < \mu \leq 0.4$. As a consequence, we could identify and analyse faculae near the limb with significantly lower B_{LOS}/μ values than what is possible from a single vantage point (e.g. that of SO/PHI), and thus extend the facular contrast curves to lower B_{LOS}/μ and μ values. This allowed us to include in our analysis the μ ranges where the maximum of the contrast curves occurs (μ_{max}, i.e. the position of the turning point of the curves, where the contrast changes its trend from increasing towards the limb to decreasing) even for low B_{LOS}/μ values.

Our results mostly confirm the trend of μ_{max} observed by Yeo et al. (2013) and Ortiz et al. (2002), in that, apart from the lowest flux densities, μ_{max} increases with decreasing B_{LOS}/μ. For these ranges we find that μ_{max} might lie closer to the limb than observations from a single point of view (e.g. that of SO/PHI, or of SDO/HMI, see Yeo et al. 2013; Ortiz et al. 2002) indicate. However, the same studies also observed an inversion of this trend around $B_{LOS}/\mu \approx 50$ G, which we cannot confirm.

Studies historically disagree on μ_{max} (see, e.g. Solanki 1993) due to several factors, including (but not limited to), the resolution of the observations, the method of identification of facular features (see Centrone & Ermolli 2003), and the systematic exclusion of features that could not be clearly identified as faculae (see Auffret & Muller 1991). The μ_{max} values computed by us still have significant uncertainties, as our study is preliminary and can be improved in multiple aspects listed below. However, the presented results suggest that analysing more and higher resolution data from two vantage points can lead to a more certain determination of μ_{max} than is possible from a single view point.

To consolidate the results presented here, different aspects of the present study need to be improved.

1. One obvious task is to extend the investigation using combined data also beyond $\mu = 0.4$, for example to close the gap in data points between $\mu = 0.4$ and 0.8 seen in Fig. 5 for $\langle B_{LOS}/\mu \rangle \leq 40$ G. This is straightforward with an increasing amount of available data, although it should be noted that the advantage of combining two vantage points decreases with increasing μ.

2. Also, improving the statistics by including more data from SO/PHI would make the results more robust. Fortunately, Solar Orbiter is still in a relatively early phase of its science mission, holding the promise of many more observation campaigns from various angles between the spacecraft, the Sun, and Earth. Therefore, we expect to significantly improve the statistics compared with the present paper.

3. SO/PHI data with higher resolution would be of great value to overcome the problem of the large pixels and the poor resolution of magnetic features (not just close to the limb). This can be achieved either by employing data acquired at smaller distances from the Sun with the SO/PHI-FDT (which also provides an opportunity for a direct study on the effect of changing the plate scale), or by using data from the SO/PHI-HRT, which will allow one to observe at an even higher resolution than SDO/HMI, especially when close to perihelion. Such data (from both SO/PHI telescopes) will be particularly valuable after deconvolution of the PSF (determined using phase diversity, see Kahil et al. 2023; Bailén et al. 2023). For the impact of PSF reconstruction on facular studies with SDO/HMI, readers can refer to Yeo et al. (2014) and Criscuoli et al. (2017).

4. The SO/PHI data employed here have been reduced on board preliminarily. The use of data reduced with improved methods is imperative. The data reduction methods of SO/PHI have already been refined beyond what was available at the time of the processing of the data for this study, and they are being continuously improved further.

These improvements will be implemented in future studies.

References

Albert, K., Hirzberger, J., Kolleck, M., et al. 2020, J. Astron. Telesc. Instrum. Syst., 6, 048004
Auffret, H., & Muller, R. 1991, A&A, 246, 264
Bailén, F., Orozco Suárez, D., Blanco Rodríguez, J., et al. 2023, A&A, submitted
Ball, W. T., Unruh, Y. C., Krivova, N. A., et al. 2012, A&A, 541, A27
Barthol, P., Gandorfer, A., Solanki, S. K., et al. 2011, Sol. Phys., 268, 1
Beeck, B., Schüssler, M., Cameron, R. H., & Reiners, A. 2015, A&A, 581, A42
Buehler, D., Lagg, A., Solanki, S. K., & van Noort, M. 2015, A&A, 576, A27
Buehler, D., Lagg, A., van Noort, M., & Solanki, S. K. 2019, A&A, 630, A86
Carlsson, M., Stein, R. F., Nordlund, Å., & Scharmer, G. B. 2004, ApJ, 610, L137
Centrone, M., & Ermolli, I. 2003, Mem. Soc. Astron. It., 74, 671
Couvidat, S., Schou, J., Hoeksema, J. T., et al. 2016, Sol. Phys., 291, 1887
Criscuoli, S., Norton, A., & Whitney, T. 2017, ApJ, 847, 93
DeForest, C. E. 2004, Sol. Phys., 219, 3
Foukal, P., Ortiz, A., & Schnerr, R. 2011, ApJ, 733, L38
Gandorfer, A., Grauf, B., Staub, J., et al. 2018, in Space Telescopes and Instrumentation 2018: Optical, Infrared, and Millimeter Wave, eds. M. Lystrup, H. A. MacEwen, G. G. Fazio, et al., SPIE Conf. Ser., 10698, 106984N
Giovanelli, R. G., & Jones, H. P. 1982, Sol. Phys., 79, 267
Howard, R. F., Harvey, J. W., & Forgach, S. 1990, Sol. Phys., 130, 295
Jafarzadeh, S., Solanki, S. K., Lagg, A., et al. 2014, A&A, 569, A105
Kahil, F., Riethmüller, T. L., & Solanki, S. K. 2019, A&A, 621, A78
Kahil, F., Gandorfer, A., Hirzberger, J., et al. 2023, A&A, 675, A61 (SO Nominal Mission Phase SI)
Keller, C. U., Schüssler, M., Vögler, A., & Zakharov, V. 2004, ApJ, 607, L59
Kobel, P., Solanki, S. K., & Borrero, J. M. 2011, A&A, 531, A112
Korpi-Lagg, M. J., Korpi-Lagg, A., Olspert, N., & Truong, H. L. 2022, A&A, 665, A141
Krivova, N. A., Solanki, S. K., Fligge, M., & Unruh, Y. C. 2003, A&A, 399, L1
Lagg, A., Solanki, S. K., Riethmüller, T. L., et al. 2010, ApJ, 723, L164
Landi Degl'Innocenti, E., & Landolfi, M. 2004, Polarization in Spectral Lines (Springer), 307
Liu, Y., Hoeksema, J. T., Scherrer, P. H., et al. 2012, Sol. Phys., 279, 295
Martínez Pillet, V., del Toro Iniesta, J. C., Álvarez-Herrero, A., et al. 2011, Sol. Phys., 268, 57
Müller, D., St. Cyr, O. C., Zouganelis, I., et al. 2020, A&A, 642, A1
Neckel, H., & Labs, D. 1994, Sol. Phys., 153, 91
Ortiz, A., Solanki, S. K., Domingo, V., Fligge, M., & Sanahuja, B. 2002, A&A, 388, 1036
Rees, D. E., & Semel, M. D. 1979, A&A, 74, 1
Schou, J., Scherrer, P. H., Bush, R. I., et al. 2012, Sol. Phys., 275, 229
Schou, J., Hirzberger, J., Orozco Suárez, D., et al. 2023, A&A, 673, A84 (SO Nominal Mission Phase SI)
Semel, M. 1967, Ann. Astrophys., 30, 513
Shapiro, A. I., Solanki, S. K., Krivova, N. A., et al. 2017, Nat. Astron., 1, 612
Solanki, S. K. 1993, Space Sci. Rev., 63, 1
Solanki, S. K., & Stenflo, J. O. 1984, A&A, 140, 185
Solanki, S. K., Montavon, C. A. P., & Livingston, W. 1994, A&A, 283, 221
Solanki, S. K., Steiner, O., Buente, M., Murphy, G., & Ploner, S. R. O. 1998, A&A, 333, 721
Solanki, S. K., Inhester, B., & Schüssler, M. 2006, Rep. Progr. Phys., 69, 563
Solanki, S. K., Barthol, P., Danilovic, S., et al. 2010, ApJ, 723, L127
Solanki, S. K., Krivova, N. A., & Haigh, J. D. 2013, ARA&A, 51, 311
Solanki, S. K., del Toro Iniesta, J. C., Woch, J., et al. 2020, A&A, 642, A11
Spruit, H. C. 1976, Sol. Phys., 50, 269
SunPy Community (Barnes, W. T., et al.) 2020, ApJ, 890, 68
Thompson, W. T. 2006, A&A, 449, 791
Yeo, K. L., Solanki, S. K., & Krivova, N. A. 2013, A&A, 550, A95
Yeo, K. L., Feller, A., Solanki, S. K., et al. 2014, A&A, 561, A22
Yeo, K. L., Solanki, S. K., Norris, C. M., et al. 2017, Phys. Rev. Lett., 119, 139902
Yeo, K. L., Solanki, S. K., Krivova, N. A., et al. 2020, Geophys. Res. Lett., 47, e2020GL090243

1 Max-Planck-Institut für Sonnensystemforschung, Justus-von-Liebig-Weg 3, 37077 Göttingen, Germany
e-mail: albert@mps.mpg.de; solanki@mps.mpg.de
2 Instituto de Astrofísica de Andalucía (IAA-CSIC), Apartado de Correos 3004, 18080 Granada, Spain
e-mail: jti@iaa.es
3 Univ. Paris-Sud, Institut d'Astrophysique Spatiale, UMR 8617, CNRS, Bâtiment 121, 91405 Orsay Cedex, France
4 Instituto Nacional de Técnica Aeroespacial, Carretera de Ajalvir, km 4, 28850 Torrejón de Ardoz, Spain
5 Universitat de València, Catedrático José Beltrán 2, 46980 Paterna-Valencia, Spain
6 Leibniz-Institut für Sonnenphysik, Schöneckstr. 6, 79104 Freiburg, Germany
7 Institut für Datentechnik und Kommunikationsnetze der TU Braunschweig, Hans-Sommer-Str. 66, 38106 Braunschweig, Germany
8 University of Barcelona, Department of Electronics, Carrer de Martí i Franquès, 1 – 11, 08028 Barcelona, Spain
9 Instituto Universitario "Ignacio da Riva", Universidad Politécnica de Madrid, IDR/UPM, Plaza Cardenal Cisneros 3, 28040 Madrid, Spain
10 Institut für Astrophysik, Georg-August-Universität Göttingen, Friedrich-Hund-Platz 1, 37077 Göttingen, Germany
11 Fraunhofer Institute for High-Speed Dynamics, Ernst-Mach-Institut, EMI, Ernst-Zermelo-Str. 4, 79104 Freiburg, Germany

Appendix A: Re-projection of SDO/HMI data onto SO/PHI's coordinate system

Figure A.1 shows B_{LOS}/μ over a selected part of the disc in both SO/PHI and SDO/HMI data, to illustrate the quality of the data alignment of magnetic features selected from the solar scene. The SDO/HMI data has been re-projected from the disc centre (where it was observed) to the coordinate system of SO/PHI, and aligned through local correlation of B_{LOS}/μ, as described in Sect. 3. In the right panels, we show B_{LOS}/μ along cross-sections marked by the corresponding lines on the maps (panels on the left). We note, that verifying the alignment is not straightforward due to the difference in the observation angle, as well as the smaller pixel size and lower noise levels in the re-projected SDO/HMI observations.

Misalignment of the pixels would lead to assigning internetwork or sunspot/pore I_c pixels to facular B_{LOS}/μ pixels. This would change the derived facular intensity contrast (by decreasing it and by shifting the curves in μ or B_{LOS}/μ), as well as increase the standard deviation of the bins, shown in Figs. 4 and 5. Based on inspection of different areas, as shown in Fig. A.1, we consider it unlikely that the misalignment of pixels is a major source of error in the contrast curves. However, a more robust distortion model allowing a more reliable alignment would certainly be of benefit for subsequent studies.
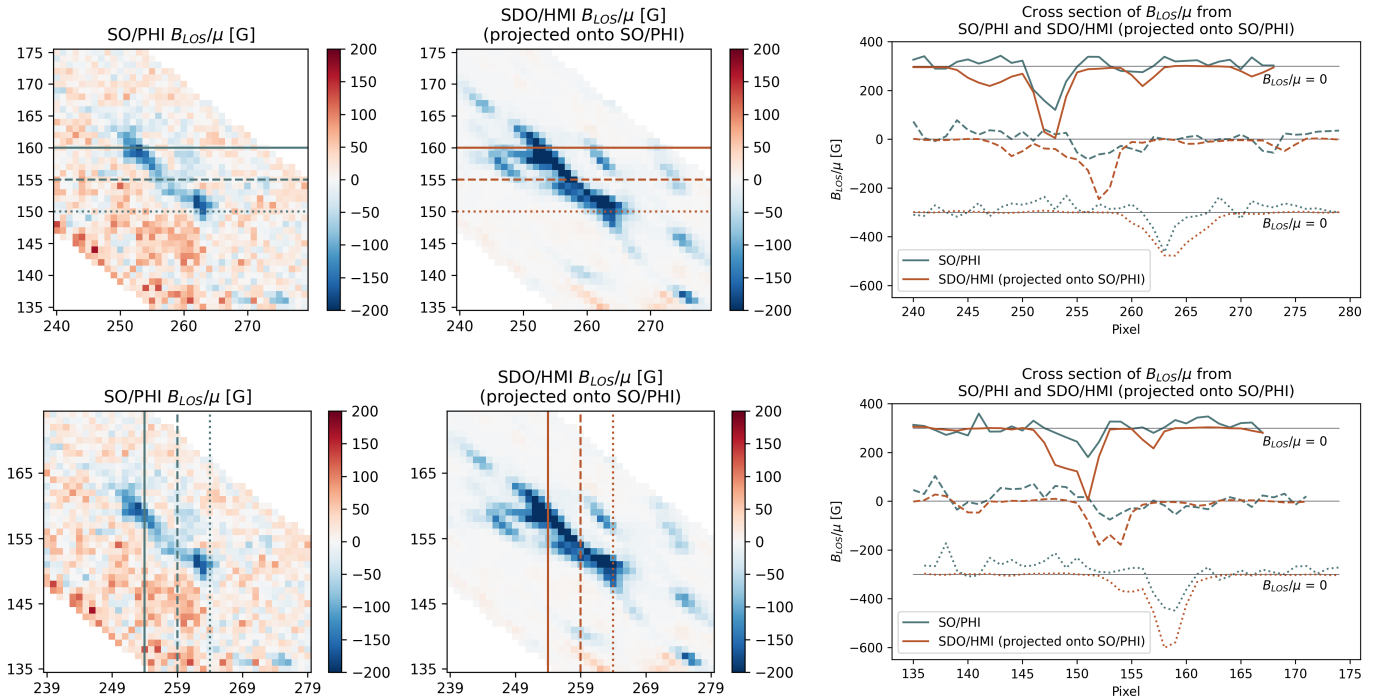

Fig. A.1. Detailed view (left column) of B_{LOS}/μ for a selected area in SO/PHI data at the limb and in SDO/HMI close to disc centre, after re-projection to the limb. The right column shows examples of B_{LOS}/μ along cross-sections marked by the lines in the maps on the left. In the right panels, the different curves are offset by 300 G in ordinate for better visibility (the respective 0 G is marked by the horizontal lines).